

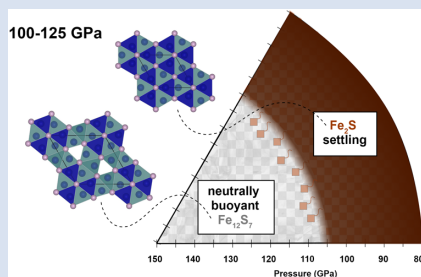
Stability of Fe₂S and Fe₁₂S₇ to 125 GPa; implications for S-rich planetary cores

C.C. Zurkowski^{1*}, B. Lavina^{2,3}, S. Chariton³, V. Prakapenka³, A.J. Campbell¹



<https://doi.org/10.7185/geochemlet.2217>

Abstract



The Fe-FeS phase relations were explored in the 22–25 wt. % S compositional range using single crystal X-ray diffraction in a laser heated diamond anvil cell. At pressures up to 125 GPa and at high temperatures, Fe₂S and Fe₁₂S₇ were determined to co-crystallise. The novel Fe₁₂S₇ compound adopts the Co₁₂P₇ structure and Fe₂S assumes the Fe₂P-type structure. Applying these results to an Fe-FeS binary phase diagram exposes a complex series of FeS phase assemblages in the 16–25 wt. % S range, whereby minor changes in S content significantly affect the crystallisation sequence of Fe-S rich planetary cores. For core compositions S-rich of the Fe₂S-Fe₁₂S₇ eutectic, the small density difference between solid Fe₁₂S₇ and Fe₂S is likely to result in the formation of a core slush rather than a gravitationally stable inner core.

Crystallisation of denser Fe₂S at eutectic conditions could then result in gravitational settling of an Fe₂S-rich inner core over time. As the Fe₂P-type Fe₂S has previously been identified forming at high temperatures to pressures as low as 22 GPa, the core crystallisation regimes determined here also elucidate that the Martian core sulfur composition must lie on the S-rich side of the Fe-Fe₃S eutectic or even the S-rich side of the Fe₃S-Fe₂S eutectic to maintain a fully molten core.

Received 29 October 2021 | Accepted 28 March 2022 | Published 11 May 2022

Introduction

Earth and other terrestrial planets are composed of silicate mantles and Fe-alloy metallic cores (e.g., McDonough and Sun, 1995; Righter and O'Brien, 2011). Sulfur easily alloys with and lowers the melting temperature of iron (Fei et al., 2000; Campbell et al., 2007; Kamada et al., 2012; Mori et al., 2017), and plays a key role in early metal-melt formation and differentiation (Murthy and Hall, 1970; Kruijer et al., 2014; Terasaki et al., 2008). Therefore, the Fe-FeS phase equilibria and eutectic melting relations relevant to the *P-T-X* conditions of a given planetary core play a significant role in the core's evolving structure as it crystallises over time.

The terrestrial planets each have different interior structures, oxidation states, and proposed core sulfur contents. Cosmochemical models and metal-silicate partitioning experiments estimate that Earth's core contains ~2 wt. % sulfur (McDonough, 2003; Suer et al., 2017), and the sulfur content of the core is limited to <6 wt. % to explain the presence of an Fe-rich inner core (Mori et al., 2017). Mercury is small and dense, with a large core-mass fraction and a reduced core composition with sulfur contents <1.5 wt. % (Smith et al., 2012; Namur et al., 2016; Genova et al., 2019). Recent analysis of Marsquakes and geodetic data from the *InSight* mission reveal that Mars' core accounts for ~½ the planet's radius and is fully molten, such that it likely has a high sulfur content (Stähler et al., 2021). In a purely Fe-S Martian core, 25 wt. % sulfur is required

to explain the observations, while in a multicomponent core with cosmochemically plausible light element concentrations, a minimum of 10–15 wt. % sulfur is required (Stähler et al., 2021). Less is known about Venus: its core is likely fully molten, due to the lack of heat release through plate tectonics (Nimmo, 2002), which lends little constraint on how the core composition contributes to the core structure.

Reflecting on the 6–360 GPa pressure range and 1.5–25 wt. % potential sulfur concentrations in the terrestrial planetary cores in our solar system alone, it is inevitable that a much wider variety of core structures and compositions exists in planetary bodies outside of our solar system. Continuing to build the Fe sulfide phase diagram with pressure, temperature and composition is critical for interpreting core crystallisation in our solar system and beyond. Here we report new findings on the high *P-T* polymorphism of Fe₂S (22 wt. % S) and the discovery of Fe₁₂S₇ (25 wt. % S) to 125 GPa, and use these findings to model the structures of planetary cores with 16–25 wt. % S.

Experimental Methods

High pressure-temperature conditions were achieved on Fe₆₆S₃₄ (by atom) samples using a laser heated diamond anvil cell. Powder and single crystal X-ray diffraction techniques were employed during heating and after temperature quenching, respectively, at beamline 13 ID-D of the Advanced Photon

1. University of Chicago, Department of the Geophysical Sciences, 5734 S Ellis Ave, Chicago, IL 60637, USA

2. X-ray Science Division, Advanced Photon Source, Argonne National Laboratory, Argonne, IL 60439, USA

3. Center for Advanced Radiation Sources, 9700 South Cass Avenue, Building 434A, Argonne, IL 60439, USA

* Corresponding author (email: czurkowski@carnegiescience.edu)



Source, Argonne National Lab. Analysis of the diffraction data is described in detail in the [Supplementary Information](#).

Synthesis and Structure Determination of Fe_2S and Fe_{12}S_7

Two high P - T experiments were conducted at 105.3 (9) GPa (values in parentheses are propagated uncertainties on the last reported digits) and quenched from 2400 (120) K and 125 (1) GPa and quenched from 2260 (140) K ([Table S-2](#)). After each heating, rotational diffraction scans were collected at various locations around the heated region to assess the phase relations. At each pressure step two distinct lattices were identified at the centre of the laser heated spot and are likely the relevant high temperature sulfides at these P - X conditions ([Fig. 1](#)).

One set of grains was indexed to a hexagonal cell with parameters $a = 5.326$ (7) Å and $c = 3.125$ (3) Å, compatible with

3 formula units of Fe_2S ([Table 1](#), [Fig. 1a](#)). The systematic absences identified for this hexagonal phase are compatible with a $P-62m$ space group, and a Fe_2P -type (Pearson symbol: $C22$, $Z = 3$) structure was solved and refined to the data ([Table 1](#), [Table S-2](#), [Fig. 1b](#)) ([Rundqvist and Jellinek, 1959](#)). This $C22$ structure, shown in [Figure 1b](#), is composed of 4 fold coordinated and 5 fold coordinated iron sites arranged into columns of edge sharing square pyramids (green) and columns of corner sharing tetrahedra (blue) linked along edges in the c direction ([Fig. 1a](#); [Appendix A-1](#)). Additional Co_2P -type and Cr_2P -type Fe_2S polymorphs were identified in the lower temperature regions of the laser heated spot after each run and discussion of their structures are provided in the [Supplementary Information](#).

The second set of grains was indexed to a hexagonal cell with $a = 7.794$ (2) Å and $c = 3.1234$ (8) Å, compatible with 1 formula unit of Fe_{12}S_7 ([Table 2](#), [Fig. 1c](#)). Crystal structure solution and refinement reveal that Fe_{12}S_7 adopts the Co_{12}P_7 structure ($P-6$, $Z = 1$) ([Zurkowski et al., 2020](#)) ([Fig. 1d](#); [Appendix A-2](#)).

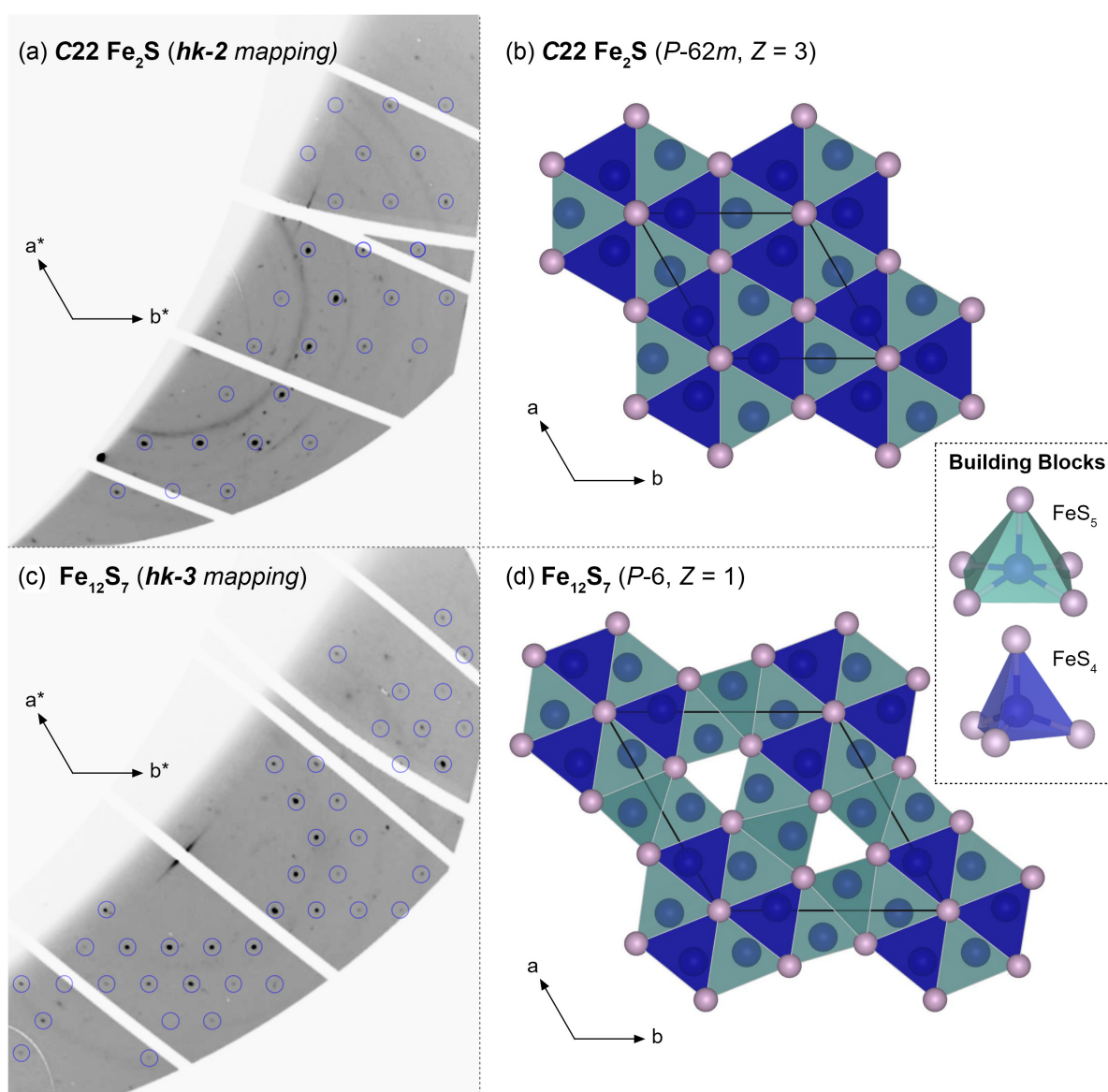


Figure 1 (a) Diffraction mapping of the hexagonal Fe_2S lattice collected at 105 GPa upon quenching from 2400 K. The reflections shown all satisfy the condition $hk-2$. (b) The crystal structure of Fe_2P -type Fe_2S (Pearson symbol $C22$). (c) Diffraction mapping of an Fe_{12}S_7 lattice identified at 105 GPa upon quenching from 2400 K. The reflections shown all satisfy the condition $hk-3$. (d) The crystal structure of Co_{12}P_7 -type Fe_{12}S_7 . The FeS_5 and FeS_4 building blocks observed in both the Fe_2S and Fe_{12}S_7 structures are shown in the centre-right inset.

Table 1 Unit cell parameters, volumes, and densities of hexagonal Fe₂S and Fe₁₂S₇ indexed at each pressure step upon temperature quenching. Values in parentheses are propagated uncertainties on the last reported digits.

| Phase | <i>P</i> (GPa) | Synthesis <i>T</i> (K) | <i>a</i> (Å) | <i>c</i> (Å) | <i>V</i> (Å ³) | <i>Z</i> | ρ (g/cm ³) |
|---------------------------------|----------------|------------------------|--------------|--------------|----------------------------|----------|-----------------------------|
| Fe ₂ S | 105.3 (9) | 2400 (120) | 5.340 (3) | 3.133 (2) | 77.38 (9) | 3 | 9.27 (1) |
| | 125 (1) | 2260 (140) | 5.282 (5) | 3.062 (4) | 74.0 (2) | | 9.69 (1) |
| Fe ₁₂ S ₇ | 105.3 (9) | 2400 (120) | 7.794 (2) | 3.1234 (8) | 164.33 (8) | 1 | 9.05 (1) |
| | 125 (1) | 2260 (140) | 7.700 (7) | 3.104 (4) | 159.4 (3) | | 9.32 (1) |

Table 2 Atomic coordinates refined for the C22 Fe₂S and Fe₁₂S₇ structure models at 105 GPa.

| Phase | Site | <i>x</i> | <i>y</i> | <i>z</i> | sof | U11 | U22 | U33 | U23 | U13 | U12 | Ueq |
|---------------------------------|-------|----------|----------|----------|-------|-------|-------|-------|-----|-----|--------|--------|
| C22 Fe ₂ S | Fe1 | 0.5990 | 0 | -1/2 | 1/4 | 0.010 | 0.010 | 0.009 | 0 | 0 | 0.0052 | 0.0095 |
| | error | 0.0008 | | | | 0.001 | 0.001 | 0.002 | | | 0.0007 | 0.0008 |
| | Fe2 | 0.2594 | 0 | 0 | 1/4 | 0.009 | 0.008 | 0.011 | 0 | 0 | 0.0041 | 0.0092 |
| | error | 0.0006 | | | | 0.001 | 0.002 | 0.001 | | | 0.0008 | 0.0007 |
| | S1 | 2/3 | 1/3 | 0 | 1/6 | 0.007 | | | | | | |
| | error | | | | | 0.001 | | | | | | |
| Fe ₁₂ S ₇ | S2 | 0 | 0 | 1/2 | 1/12 | 0.011 | | | | | | |
| | error | | | | | 0.002 | | | | | | |
| | Fe1 | 0.0151 | 0.2549 | 0 | 1/2 | 0.010 | 0.020 | 0.014 | 0 | 0 | 0.005 | 0.0159 |
| | error | 0.0006 | 0.0006 | | | 0.001 | 0.002 | 0.001 | | | 0.001 | 0.0008 |
| | Fe2 | 0.1335 | 0.6233 | 0 | 1/2 | 0.009 | 0.010 | 0.014 | 0 | 0 | 0.004 | 0.0112 |
| | error | 0.0006 | 0.0005 | | | 0.001 | 0.001 | 0.002 | | | 0.001 | 0.0009 |
| | Fe3 | 0.2324 | 0.2178 | 1/2 | 1/2 | 0.032 | 0.024 | 0.012 | 0 | 0 | 0.024 | 0.0185 |
| | error | 0.0006 | 0.0007 | | | 0.002 | 0.002 | 0.001 | | | 0.002 | 0.0008 |
| | Fe4 | 0.5170 | 0.1334 | 1/2 | 1/2 | 0.009 | 0.009 | 0.014 | 0 | 0 | 0.005 | 0.0106 |
| | error | 0.0005 | 0.0005 | | | 0.001 | 0.001 | 0.002 | | | 0.001 | 0.0009 |
| | S5 | 0.1638 | 0.4476 | 1/2 | 1/2 | 0.011 | | | | | | |
| | error | 0.0008 | 0.0010 | | | 0.001 | | | | | | |
| S6 | 0.446 | 0.281 | 0 | 1/2 | 0.013 | | | | | | | |
| error | 0.001 | 0.001 | | | 0.001 | | | | | | | |
| S7 | 0 | 0 | 0 | 1/6 | 0.020 | | | | | | | |
| error | | | | | 0.002 | | | | | | | |

The Co₁₂P₇ structure is closely related to the C22 Fe₂S structure, in that it is composed of the same building blocks arranged into similar edge-sharing columns, but an increased ratio of square pyramid to tetrahedral building blocks results in the formation of trigonal channels along the *c* direction in Fe₁₂S₇ (Fig. 1d). Previous studies have asserted that this structure is not likely stable in Fe-rich systems as it is composed of a majority 5 fold coordinated sites (Dhahri, 1996), but this work reveals that this structure stabilises in the Fe-S systems with sufficient pressure and temperature.

Crystallisation Sequences in S-rich Planetary Cores

The novel Fe₂P-type Fe₂S (22 wt. % S) and Co₁₂P₇-type Fe₁₂S₇ (25 wt. % S) phases were then used to construct an updated binary *X-T* phase diagram between 100 and 125 GPa (Fig. 2). The Fe-rich portion (<16 wt. % S) of this phase diagram has been characterised at these conditions previously (e.g., Kamada *et al.*, 2012; Mori *et al.*, 2017), but the addition of this study exposes the complexity of Fe-S phase assemblages in the limited 16–25 wt. % S range: Fe₃S + Fe₂S (16–22 wt. %) and Fe₂S + Fe₁₂S₇ (22–25 wt. %) (Fig. 2a).

As the structures of planetary cores are dictated by the density difference between the crystallising phases and remaining liquid, these Fe-S phase relations determine the possible S-rich core crystallisation regimes for an approximately Venus-sized planet (Aitta, 2012), such as the rocky exoplanet TRAPPIST-1e ($R_{T1e} = 0.96 \times R_{Venus}$) (Grimm *et al.*, 2018). The visualisations in Figure 2b depict the intricacies of these S-rich crystallising cores. With core compositions ranging from 16–22 wt. % sulfur, two crystallisation models are possible: Fe₃S may crystallise into the inner core leaving a lower density, more S-rich liquid outer core or, for more S-rich compositions, Fe₂S would be the crystallising phase from a more Fe-rich liquid, producing gravitationally buoyant 'snow' that would remix and not produce a solid inner core (Fig. 2b; Scenarios 1, 2).

Then for 22–25 wt. % sulfur concentrations, further variations are possible. A gravitationally stable Fe₂S-rich inner core could form for core compositions on the Fe-rich side of the Fe₂S-Fe₁₂S₇ eutectic (Fig. 2b; Scenario 3). Alternatively, for more S-rich compositions shown in Scenario 4 in Figure 2b, the crystallisation of Fe₁₂S₇ from a more Fe-rich liquid could result in a neutrally buoyant slush due to the near equivalent densities of an Fe₂S-rich liquid and Fe₁₂S₇ solid. At 105 GPa, a ~2.5 % volume increase of Fe₂S upon melting results in equivalent solid Fe₁₂S₇ and liquid Fe₂S densities. As changes in volume from

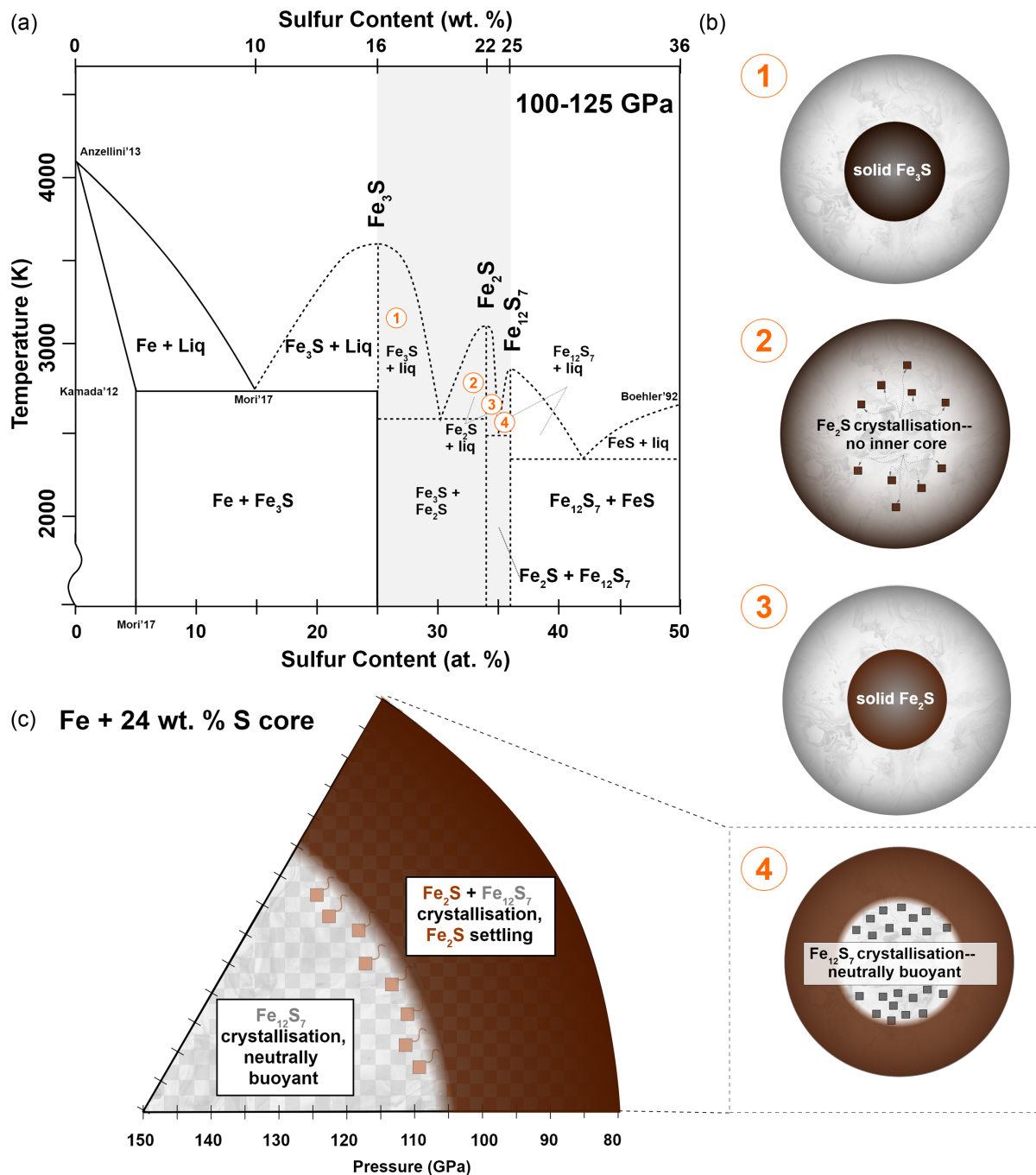


Figure 2 (a) Phase diagram for the Fe-FeS system between 100–125 GPa inferred from this study in the 16–26 wt. % S (25–36 at. %) range along with previous studies: Fe and FeS melting temperatures were taken from Anzellini *et al.* (2013) and Boehler (1992), and eutectic melting temperature and composition in the Fe-Fe₃S system are based on Kamada *et al.* (2012) and Mori *et al.* (2017). (b) In the 16–25 wt. % S range, four core crystallisation scenarios are possible depending on the crystallising phase and the density difference between it and the remaining core liquid. In case 4 in (b), the minimal density difference between solid Fe₂S and an Fe₂S-rich liquid, may result in a neutrally buoyant solid and liquid and the formation of a core slush. (c) A crystallisation model of an Fe + 24 wt. % S core spanning 80–150 GPa indicates that Fe₂S may begin to crystallise with Fe₁₂S₇ around 115 GPa, causing the denser Fe₂S to precipitate out and settle downwards.

15 % have been estimated upon melting in previous studies of iron-rich systems (Anderson 2003; Kuwayama *et al.*, 2020), these values credit the possibility of neutrally buoyant rather than density settling crystallisation in such an S-rich core. Once eutectic temperature and composition is reached in this system, the crystallisation of both Fe₁₂S₇ and Fe₂S will result in solidification of an inner core over time.

A core crystallisation model of an S-rich core was then constructed to further assess this scenario (Fig. 2c). The model

begins with a fully molten exoplanetary core with Fe + 24 wt. % S composition that spans an arbitrary pressure range of 80–50 GPa with radius of 950 km. These pressure-depth values were assumed using a similar relationship as constrained for Earth’s core. Equations of state of Fe and Fe₂S in this pressure range were then used convert from weight percent to volume percent of sulfur in the bulk starting liquid (Dewaele *et al.*, 2006; Zurkowski *et al.*, 2022). The model proceeds by crystallising along the S-rich side of the Fe₁₂S₇ eutectic in radial shells,

assuming temperatures are at the liquidus in each step and following the approximate Fe_{12}S_7 liquidus in Figure 2a. The volume fractions of Fe and S were then deducted from the remaining core liquid and the S content of the core liquid was recalculated. For this model core, eutectic conditions would be met around 115 GPa, resulting in the co-crystallisation of a denser Fe_2S with Fe_{12}S_7 (Fig. 2c). Depending on the dynamics of a specific iron sulfide core, further texturing of this multiphase solid inner core would be possible.

Applications for the Martian Core

Marsquake and geodetic data obtained from the recent *InSight* mission on Mars indicates a large, fully molten core requiring more sulfur-rich core compositions than previously thought (Stähler *et al.*, 2021). As grains of C22 Fe_2S have also been synthesised at 22 GPa and 1300 K (Koch-Müller *et al.*, 2002), it is likely that the C22 Fe_2S high temperature stability field extends from at least 19–125 GPa; encompassing pressures relevant to the Martian core (18–40 GPa) (Stähler *et al.*, 2021). Fe_3S is also known to be stable at the pressures spanning the Martian core; therefore, models of an iron sulfide Martian core may involve crystallisation of Fe_3S and/or Fe_2S , like the higher pressure phase diagram in Figure 2a. The regions of the phase diagram in Figure 2a that are Fe-rich of Fe_2S may therefore be generally applied to assess possible core S contents to sustain a molten core. Based on these core-structure models (Fig. 2), the Martian core sulfur composition must lie either on the S-rich side of the Fe- Fe_3S eutectic, such that Fe_3S is the crystallising phase from a more Fe-rich liquid, or even S-rich of the Fe_3S - Fe_2S eutectic, such that Fe_2S is crystallising from a denser Fe-S liquid. Core compositions more sulfur-rich than Fe_2S are geochemically unlikely (Steenstra and van Westrenen, 2018).

Conclusions

Here we present the novel characterisation of Fe_2S and Fe_{12}S_7 from *in situ* X-ray diffraction experiments conducted up to 125 GPa and apply these findings to exoplanetary core crystallisation regimes in the 16–25 wt. % sulfur range. The Fe_3S - Fe_2S - Fe_{12}S_7 phase stabilities based on core sulfur contents result in intricate core solidification structures including: gravitationally stable inner core crystallisation, low density sulfide snow and remixing in a sustained molten core, and neutrally buoyant sulfide crystallisation forming a core slush. As the stability fields of Fe_3S and Fe_2S also extend as low as 21 GPa, the phase relations Fe-rich of Fe_2S were generally applied to the molten Martian core to constrain that its sulfur contents must be S-rich of the Fe- Fe_3S eutectic or S-rich of the Fe_3S - Fe_2S eutectic. The presented experimental results and core crystallisation models highlight the sensitivity of core structure to sulfur content and the utility of the Fe-FeS phase relationships for interpreting seismically detected core structures.

Acknowledgments

Portions of this work were performed at GeoSoilEnviroCARS (The University of Chicago, Sector 13), Advanced Photon Source (APS), Argonne National Laboratory. GeoSoilEnviroCARS is supported by the National Science Foundation - Earth Sciences (EAR - 1634415). This research used resources of the Advanced Photon Source, a U.S. Department of Energy (DOE) Office of Science User Facility operated for the DOE Office of Science by Argonne National Laboratory under Contract No. DE-AC02-06CH11357. Use of the COMPRES-

GSECARS gas loading system was supported by COMPRES under NSF Cooperative Agreement EAR-1606856 and by GSECARS through NSF grant EAR-1634415 and DOE grant DE-FG02-94ER14466. This research used resources of the Advanced Photon Source, a U.S. Department of Energy (DOE) Office of Science User Facility operated for the DOE Office of Science by Argonne National Laboratory under Contract No. DE-AC02-06CH11357. This material is based upon work supported by a National Science Foundation Graduate Research Fellowship to CCZ. This work was also supported by the National Science Foundation by grant EAR-1651017 to AJC.

Editor: Anat Shahar

Additional Information

Supplementary Information accompanies this letter at <https://www.geochemicalperspectivesletters.org/article2217>.



© 2022 The Authors. This work is distributed under the Creative Commons Attribution 4.0 License, which permits unrestricted use, distribution, and reproduction in any medium, provided the original author and source are credited. Additional information is available at <http://www.geochemicalperspectivesletters.org/copyright-and-permissions>.

Cite this letter as: Zurkowski, C.C., Lavina, B., Chariton, S., Prakapenka, V., Campbell, A.J. (2022) Stability of Fe_2S and Fe_{12}S_7 to 125 GPa; implications for S-rich planetary cores. *Geochem. Persp. Let.* 21, 47–52. <https://doi.org/10.7185/geochemlet.2217>

References

- AITTA, A. (2012) Venus' internal structure, temperature and core composition. *Icarus* 218, 967–974. <https://doi.org/10.1016/j.icarus.2012.01.007>
- ANDERSON, O.L. (2003) The Three-Dimensional Phase Diagram of Iron. In: DEHANT, V., CREAMER, K.C., KARATO, S.-I., ZATMAN, S. (Eds.) *Earth's Core: Dynamics, Structure, Rotation*. American Geophysical Union, Washington, D.C., 83–103. <https://doi.org/10.1029/GD031>
- ANZELLINI, S., DEWAELE, A., MEZOUAR, M., LOUBEYRE, P., MORARD, G. (2013) Melting of iron at Earth's inner core boundary based on fast X-ray diffraction. *Science* 340, 464–466. <https://doi.org/10.1126/science.1233514>
- BOEHLER, R. (1992) Melting of the Fe-FeO and the Fe-FeS systems at high pressure: Constraints on core temperatures. *Earth and Planetary Science Letters* 111, 217–227. [https://doi.org/10.1016/0012-821X\(92\)90180-4](https://doi.org/10.1016/0012-821X(92)90180-4)
- CAMPBELL, A.J., SEAGLE, C.T., HEINZ, D.L., SHEN, G., PRAKAPENKA, V.B. (2007) Partial melting in the iron-sulfur system at high pressure: A synchrotron X-ray diffraction study. *Physics of the Earth and Planetary Interiors* 162, 119–128. <https://doi.org/10.1016/j.pepi.2007.04.001>
- DEWAELE, A., LOUBEYRE, P., OCCELLI, F., MEZOUAR, M., DOROGOKUPETS, P.I., TORRENT, M. (2006) Quasihydrostatic Equation of State of Iron above 2 Mbar. *Physical Review Letters* 97, 215504. <https://doi.org/10.1103/PhysRevLett.97.215504>
- DHAHRI, E. (1996) Etude des problèmes d'ordre et de stabilité dans les phases $\text{Ln}_2\text{M}_{12}\text{X}_7$ (terre rare-métal de transition-non métal). *Journal of Physics: Condensed Matter* 8, 4351. <https://doi.org/10.1088/0953-8984/8/24/004>
- FEI, Y., LI, J., BERTEKA, C.M., PREWITT, C.T. (2000) Structure type and bulk modulus of Fe_3S , a new iron-sulfur compound. *American Mineralogist* 85, 1830–1833. <https://doi.org/10.2138/am-2000-11-1229>
- GENOVA, A., GOOSSENS, S., MAZARICO, E., LEMOINE, F.G., NEUMANN, G.A., KUANG, W., SABAKA, T.J., HAUCK, S.A., SMITH, D.E., SOLOMON, S.C., ZUBER, M.T. (2019) Geodetic Evidence That Mercury Has A Solid Inner Core. *Geophysical Research Letters* 46, 3625–3633. <https://doi.org/10.1029/2018GL081135>
- GRIMM, S.L., DEMORY, B.-O., GILLON, M., DORN, C., AGOL, E., *et al.* (2018) The nature of the TRAPPIST-1 exoplanets. *Astronomy & Astrophysics* 613, A68. <https://doi.org/10.1051/0004-6361/201732233>



- KAMADA, S., OHTANI, E., TERASAKI, H., SAKAI, T., MIYAHARA, M., OHISHI, Y., HIRAO, N. (2012) Melting relationships in the Fe–Fe₃S system up to the outer core conditions. *Earth and Planetary Science Letters* 359–360, 26–33. <https://doi.org/10.1016/j.epsl.2012.09.038>
- KOCH-MÜLLER, M., FEI, Y., WIRTH, R., BERTKA, C.M. (2002) Characterization of high-pressure iron-sulfur compounds. *Lunar and Planetary Science Conference XXXIII*, Houston, TX, abstract no. 1424.
- KRUIJER, T.S., TOUBOUL, M., FISCHER-GÖDDE, M., BERMINGHAM, K.R., WALKER, R.J., KLEINE, T. (2014) Protracted core formation and rapid accretion of protoplanets. *Science* 344, 1150–1154. <https://doi.org/10.1126/science.1251766>
- KUWAYAMA, Y., MORARD, G., NAKAJIMA, Y., HIROSE, K., BARON, A.Q.R., KAWAGUCHI, S.I., TSUCHIYA, T., ISHIKAWA, D., HIRAO, N., OHISHI, Y. (2020) Equation of State of Liquid Iron under Extreme Conditions. *Physical Review Letters* 124, 165701. <https://doi.org/10.1103/PhysRevLett.124.165701>
- MCDONOUGH, W.F., SUN, S.S. (1995) The composition of the Earth. *Chemical Geology* 120, 223–253. [https://doi.org/10.1016/0009-2541\(94\)00140-4](https://doi.org/10.1016/0009-2541(94)00140-4)
- MCDONOUGH, W.F. (2003) 2.15 - Compositional Model for the Earth's Core. In: HOLLAND, H.D., TUREKIAN, K.K. (Eds.) *Treatise on Geochemistry, Volume 2: The Mantle and Core*. First Edition, Elsevier, Amsterdam, 547–568. <https://doi.org/10.1016/B0-08-043751-6/02015-6>
- MORI, Y., OZAWA, H., HIROSE, K., SINMYO, R., TATENO, S., MORARD, G., OHISHI, Y. (2017) Melting experiments on Fe–Fe₃S system to 254 GPa. *Earth and Planetary Science Letters* 464, 135–141. <https://doi.org/10.1016/j.epsl.2017.02.021>
- MURTHY, V.R., HALL, H.T. (1970) The chemical composition of the Earth's core: Possibility of sulphur in the core. *Physics of the Earth and Planetary Interiors* 2, 276–282. [https://doi.org/10.1016/0031-9201\(70\)90014-2](https://doi.org/10.1016/0031-9201(70)90014-2)
- NAMUR, O., CHARLIER, B., HOLTZ, F., CARTIER, C., MCCAMMON, C. (2016) Sulfur solubility in reduced mafic silicate melts: Implications for the speciation and distribution of sulfur on Mercury. *Earth and Planetary Science Letters* 448, 102–114. <https://doi.org/10.1016/j.epsl.2016.05.024>
- NIMMO, F. (2002) Why does Venus lack a magnetic field? *Geology* 30, 987–990. [https://doi.org/10.1130/0091-7613\(2002\)030<0987:WDVLAM>2.0.CO;2](https://doi.org/10.1130/0091-7613(2002)030<0987:WDVLAM>2.0.CO;2)
- RIGHTER, K., O'BRIEN, D.P. (2011) Terrestrial planet formation. *Proceedings of the National Academy of Sciences* 108, 19165–19170. <https://doi.org/10.1073/pnas.1013480108>
- RUNDOVIST, S., JELLINEK, F. (1959) The structures of Ni₃Si₂B, Fe₂P and some related phases. *Acta Chemica Scandinavica* 13, 425–432. <https://doi.org/10.3891/acta.chem.scand.13-0425>
- SMITH, D.E., ZUBER, M.T., PHILLIPS, R.J., SOLOMON, S.C., HAUCK, S.A., *et al.* (2012) Gravity Field and Internal Structure of Mercury from MESSENGER. *Science* 336, 214–217. <https://doi.org/10.1126/science.1218809>
- STÄHLER, S.C., KHAN, A., BANERDT, W.B., LOGNONNÉ, P., GIARDINI, D., *et al.* (2021) Seismic detection of the Martian core. *Science* 373, 443–448. <https://doi.org/10.1126/science.abi7730>
- STEENSTRA, E.S., VAN WESTRENE, W. (2018) A synthesis of geochemical constraints on the inventory of light elements in the core of Mars. *Icarus* 315, 69–78. <https://doi.org/10.1016/j.icarus.2018.06.023>
- SUER, T.A., SIEBERT, J., REMUSAT, L., MENGUY, N., FIQUET, G. (2017) A sulfur-poor terrestrial core inferred from metal–silicate partitioning experiments. *Earth and Planetary Science Letters* 469, 84–97. <https://doi.org/10.1016/j.epsl.2017.04.016>
- TERASAKI, H., FROST, D.J., RUBIE, D.C., LANGENHORST, F. (2008) Percolative core formation in planetesimals. *Earth and Planetary Science Letters* 273, 132–137. <https://doi.org/10.1016/j.epsl.2008.06.019>
- ZURKOWSKI, C., LAVINA, B., CHARITON, S., TKACHEV, S., PRAKAPENKA, V., CAMPBELL, A. (2020). The novel high-pressure/high-temperature compound Co₁₂P₇ determined from synchrotron data. *Acta Crystallographica Section E: Crystallographic Communications* 76, 1665–1668. <https://doi.org/10.1107/S2056989020012657>
- ZURKOWSKI, C.C., LAVINA, B., BRAUSER, N.M., DAVIS, A.H., CHARITON, S., TKACHEV, S., GREENBERG, E., PRAKAPENKA, V.B., CAMPBELL, A.J. (2022) Pressure-induced C23–C37 transition and compression behavior of orthorhombic Fe₂S to Earth's core pressures and high temperatures. *American Mineralogist*, in press. <https://doi.org/10.2138/am-2022-8187>

Stability of Fe₂S and Fe₁₂S₇ to 125 GPa; implications for S-rich planetary cores

C.C. Zurkowski, B. Lavina, S. Chariton, V. Prakapenka, A.J. Campbell

Supplementary Information

The Supplementary Information includes:

- Experimental Methods
- Structural Relationship of the Fe₂S Polymorphs and Fe₁₂S₇
- Tables S-1 and S-2
- Figures S-1 to S-3
- Appendices A-1 to A-4
- Supplementary Information References

Experimental Methods

The high pressure and temperature conditions for iron sulfide synthesis were achieved in a laser-heated diamond anvil cell (DAC). The starting material used in this study consisted of Fe (>99.9 %, <10 μm, Alfa Aesar) powder and iron sulfide (FeS, 99.99 %, Alfa Aesar) mixed into a ratio of 1g Fe to 1.78 g FeS (referred herein to as Fe₆₆S₄₄). The starting material was homogenised in a pestle and mortar for one hour in alcohol, dried, and then mixed dry for a short time. This final dry mixing accounts for density separation during alcohol evaporation and is conducted for a short duration to limit Fe-oxidation. The material was then compressed into foils between two ungasketed diamond anvils prior to loading.

Pressure was generated using short symmetric and BX-90-type diamond anvil cells equipped with Bohler-Almax conical diamonds and seats. Diamonds with 150 μm culets that beveled to 300 μm were used. Sixty-micron sample chambers drilled out of preindented rhenium gaskets were each loaded with a sample foil placed between layers of KCl pressure transmitting medium. The loaded samples were finally baked at 120 °C for 30 minutes prior to pressurisation. During compression, the equation of state of KCl (Dewaele *et al.*, 2012) was used to monitor pressure. The agreement between measured unit-cell parameters and structural refinement models for multiple grains of each phase in this study, support that deviatoric strain from the quenched KCl medium did not play a major role in the observed structural geometries and did not inhibit structural analysis.

Double sided laser heating of the pressurised samples was conducted at beamline 13-ID-D (GeoSoilEnviroCARS) of the Advanced Photon Source, Argonne National Laboratory. The lasers were aligned to the X-ray beam using the fluorescence of the KCl insulator (Prakapenka *et al.*, 2008). Lasers shaped with ~ 15 μm flat tops were used and temperature was measured spectroradiometrically based on the thermal emission from the central 6 μm diameter of the laser heated spot (Heinz and Jeanloz, 1987). To account for temperature gradients within the sample chamber, a 3 % correction was applied based on Campbell *et al.*, (2007, 2009). The samples were heated in ~ 30 minute cycles in the 105–125 GPa pressure range. Each sample location was heated once. Two heating experiments were carried out in this study. Run 1 was conducted on the $\text{Fe}_{66}\text{S}_{34}$ starting composition at 105.3 (9) GPa (values in parentheses are propagated uncertainties on the last reported digits) and quenched from 2400 (120) K. The sample was then pressurised to 125 (1) GPa and heated to 2260 (140) K prior to quenching in Run 2. A summarisation of the experimental conditions and instrument parameters used in this study is given in Table S-1.

Upon quenching at each pressure, X-ray diffraction was conducted at beamlines 13-ID-D (GeoSoilEnviroCARS) of the Advanced Photon Source, Argonne National Laboratory. Diffraction measurements were collected with a 2 μm by 3 μm full width at half maximum (FWHM) incident X-ray beam at 42 keV on a CdTe 1M Pilatus detector (Table 1). Around the centre of the laser heated spots, 10×10 μm diffraction maps were collected in 3 μm steps to assess the regions of optimal grain growth. Centred at selected map locations, the sample was rotated across a $\pm 30^\circ$ angular range, as diffraction images were collected in 0.5° steps. X-ray exposure time of 2–4 s were used during the rotational step scans. Due to the small size of the sample chambers, ~ 30 μm at target pressures, diffraction from the rhenium gasket was also observed in the rotational scans.

Grains of Fe_2S and Fe_{12}S_7 were identified in the reciprocal space and the reflections from each grain were isolated from reflections associated with other sulfide grains, iron, rhenium, KCl, and diamond. The target phases were indexed in the reciprocal space and the intensities of the reflections were integrated across the rotational scan using CrysAlis Pro (Rigaku Oxford Diffraction, 2018). The unit-cell parameters and structure factors were then implemented into the SHELXT structure solution program (Sheldrick, 2015a) and the atomic coordinates and displacement parameters were refined for each structure using SHELXL2014/7 (Sheldrick, 2014, 2015b). Raw diffraction images were examined and integrated using Dioptas (Prescher and Prakapenka, 2015) and VESTA was used for structure model visualisation and graphical renderings of the iron sulfides examined in this study.

Several components of high P - T synthesis do limit the capability to structurally solve and refine these crystal structures; namely, limited angular sample access in the diamond-anvil cell, overlap in diffraction angles of target phases with diffraction from other grains; rhenium; and the KCl insulator, and the volume of the grain illuminated by the X-ray beam. Despite these challenges, sufficient reflections were obtained to structurally solve and refine structure models for the Fe-sulfide phases observed in this study (Table S-2). For the refinement models shown in Table S-2, an independent-reflection-to-parameter ratio greater than 6 was maintained, a value typically suggesting that a sufficient number of reflections were collected for the number of refined parameters in the structure models at these high-pressure conditions (*e.g.*, Lavina *et al.*, 2014). The structures were refined with anisotropic displacement parameters on the metal atoms if enough reflections were collected and a significant improvement to the refinement model was observed. Alternatively, in the case of limited reflections or when adding anisotropic displacement to the metal sites did not result in a significant



change in the model quality, all sites were refined with isotropic displacement parameters. The errors on metal site occupancies are provided in Table S-2 for each refinement model and support the reported stoichiometries for the Fe-sulfides analysed. CIF files for the refined structures (Table S-2) are provided in the appendices of this work.

Structural relationship of the Fe₂S polymorphs and Fe₁₂S₇

Two high *P-T* experiments were conducted: Runs 1 and 2 were performed at 105.3 (9) GPa and quenched from 2400 (120) K and 125 (1) GPa and quenched from 2260 (140) K, respectively (Table S-2). After each heating, rotational diffraction scans were collected at various locations around the heated region to assess the phase relations. At the centre of the laser heated spot, hexagonal Fe₂S and Fe₁₂S₇ were synthesised (Fig. 1); however, grains of C23 Fe₂S (Co₂P-type, *Pnma*, *Z* = 4). and Fe₁₂S₇ were identified in the lower temperature regions of the laser heated spot (Fig. S-1, Table 1) (Zurkowski *et al.*, 2022). In Run 2, similar results were obtained (Table S-2), and additionally, a body-centred orthorhombic lattice with parameters *a* = 5.382 (1) Å, *b* = 6.103 (4) Å, *c* = 9.098 (4) Å (Fig. S-1, Table S-2) was synthesised. The volume of this lattice is compatible with 12 formula units of Fe₂S. Grains of C23 Fe₂S were also identified within the laser-heated region (Table 2).

Our crystal-chemical analyses across the laser heated spot after each heating cycle, suggests that the Co₂P-type, C23 Fe₂S is a low-temperature polymorph while the Fe₂P-type, C22 Fe₂S is a high-temperature polymorph. Agreeably, previous studies have observed the C23 structure as a lower temperature *M₂X* polymorph of C22 *M₂X* phases (Ellner and Mittemeijer, 2001). While the *P-T* conditions in Runs 1 and 2 suggest that temperatures within the laser-heated region cross the C23–C22 thermal boundary, the diffraction patterns collected after Run 2 mainly consist of a larger, body-centred orthorhombic Fe₂S lattice (Table S-2, Fig. S-1). The observed reflections of the unknown phase constrain an *Imm2* space group, and structure was solved and refined to a Cr₂P-type Fe₂S (Table 2; Figs. 2c, S-2; Appendix A-3) (Artigas *et al.*, 1996). This structure can be viewed as a slight shifting of the polyhedra in the C22 and C23 structures with polyhedral symmetry that is transitional between the C23 and C22 structures (Figs. S-2, S-3). The Cr₂P-type structure has previously been reported as a low temperature modification of the C22 structure (Artigas *et al.*, 1996). In the Fe-S system, however, observations of the Cr₂P-type Fe₂S near the C23–C22 *P-T* boundary, suggests that Cr₂P-type Fe₂S is a transitional phase forming as the polyhedra of the C23 structure shift into the C22 structure. The deviation from full occupancy for the Fe and S sites refined in the Cr₂P-type Fe₂S structure models (Table 2) are larger than that observed for the other phases examined in this study, suggesting that the Cr₂P-type Fe₂S grains were not well formed and may be metastable. Furthermore, diffraction observed from this phase shows clustering of small grains supporting that the single crystals are not well formed (Fig. S-1). The possibilities that Cr₂P-type Fe₂S is an equilibrium phase or a distortion that formed on quench cannot be ruled out and require further experiments.

Fe₁₂S₇ is observed in all heating cycles to adopt a hexagonal structure with a *P-6* space group. The structure was solved and refined to the Co₁₂P₇ structure (*Z* = 1) (Zurkowski *et al.*, 2022) (Figs. 1, S-2, Appendix A-2). All sites are fully occupied within an error of 6 %, ruling out the Cr₁₂P₇ structure (Chun and Carpenter, 1987). The Co₁₂P₇ structure is closely related to the C22, C23 and Cr₂P-type Fe₂S structures, in that it is composed of columns of edge sharing FeS₅ square pyramids (green) and columns of corner sharing



FeS₄ tetrahedra (blue) linked along edges along the *c* direction. Fe₁₂S₇ has an increased ratio of square pyramid to tetrahedral building blocks compared to the Fe₂S polymorphs, resulting in the formation of trigonal channels along the *c* direction (Figs. S-2, S-3). The interatomic distances in Fe₁₂S₇ are comparable with those observed in Co₁₂P₇ and the Fe₂S polymorphs (Zurkowski *et al.*, 2022) (Fig. S-3). It was previously thought that Fe, Ni, and Co would not occupy this structure as it is composed of a majority 5-fold coordinated sites (Dharhi 1996), but this work and the synthesis of Co₁₂P₇ (Zurkowski *et al.*, 2022) proves that this structure stabilises in the Co-P and Fe-S systems with sufficient pressure and temperature.

Supplementary Tables

Table S-1 Experimental conditions and instrument parameters used for the diffraction data collected in this study. Values in parentheses are propagated uncertainties on the last reported digits.

| | Run 1 | Run 2 |
|--|----------------------------------|------------|
| Starting composition (at. %) | Fe ₆₆ S ₃₄ | |
| Pressure (GPa) | 105.3 (9) | 125 (1) |
| Synthesis Temperature (K) | 2400 (120) | 2260 (140) |
| Synthesis Beamline | 13IDD @ APS | |
| Collection Temperature (K) | 296 | |
| Collection Station | 13IDD @ APS | |
| Radiation type | synchrotron | |
| λ (Å) | 0.2952 | |
| Beam size (FWHM) horizontal × vertical (µm) | 2 × 3 | |
| Detector | CdTe 1M Pilatus | |
| Omega range (°), step size (°), exposure time (s) | ±30, 0.5, 2 | |



Table S-2 Experimental, reduction and refinement parameters for each grain analysed in this study. Values in parentheses are propagated uncertainties on the last reported digits.

| Phase Sample Name | Co ₁₂ P ₇ -type Fe ₁₂ S ₇ | | C22 Fe ₂ S | | |
|--|---|--------------------------|--|--------------------------|--------------------------|
| | C133 P1 map 26 | C133 P2 map 26 | C133 P1 map 33 | C133 P1 map 26 | C133 P2 map 37 |
| Synthesis | | | | | |
| Run # | 1 | 2 | 1 | 1 | 2 |
| Pressure (GPa) | 105.3 (9) | 125 (1) | 105.3 (9) | 105.3 (9) | 125 (1) |
| Synthesis Temperature (K) | 2400 (120) | 2260 (140) | 2400 (120) | 2400 (120) | 2260 (140) |
| Symmetry | Hexagonal, <i>P</i> -6, <i>Z</i> = 1 | | Hexagonal, <i>P</i> -62 <i>m</i> , <i>Z</i> = 3 | | |
| <i>a</i> (Å) | 7.794 (2) | 7.706 (3) | 5.340 (3) | 5.326 (7) | 5.282 (5) |
| <i>b</i> (Å) | | | | | |
| <i>c</i> (Å) | 3.1234 (8) | 3.103 (1) | 3.133 (2) | 3.125 (3) | 3.062 (4) |
| <i>V</i> (Å ³) | 164.33 (8) | 159.6 (1) | 77.38 (9) | 76.8 (2) | 74.0 (2) |
| Reduction | | | | | |
| No. of measured, independent, and observed [<i>I</i> > 2σ(<i>I</i>)] reflections | 386, 263, 226 | 357, 285, 229 | 142, 83, 79 | 135, 80, 69 | 128, 72, 71 |
| <i>R</i> _{int} , <i>R</i> _{sigma} | 0.014, 0.014 | 0.011, 0.0210 | 0.031, 0.017 | 0.058, 0.456 | 0.014, 0.015 |
| Refinement | | | | | |
| <i>R</i> [<i>F</i> ² > 2σ(<i>F</i> ²)], <i>wR</i> (<i>F</i> ²), <i>S</i> | 0.048, 0.148, 1.16 | 0.039, 0.109, 1.05 | 0.041, 0.092, 1.33 | 0.056, 0.128, 1.11 | 0.059, 0.160, 1.30 |
| No. of reflections | 263 | 285 | 83 | 80 | 72 |
| No. of parameters | 32 | 32 | 11 | 11 | 11 |
| Δρ _{max} , Δρ _{min} (e Å ⁻³) | 2.60, -1.70 | 2.26, -1.64 | 1.15, -1.19 | 1.31, -1.89 | 2.17, -2.25 |
| Error on site occupancies | 6 % | 6 % | 2 % | 7 % | 3 % |

Table S-2 continued.

| Phase Sample Name | C23 Fe ₂ S | | | Cr ₂ P-type Fe ₂ S | |
|--|--------------------------------------|--------------------------|---------------------------|--|---------------------------|
| | C133 P1 map 33 | C133 P2 map 26 | C133 P2 map 38 | C133 P2 map 36 | C133 P2 map 37 |
| Synthesis | | | | | |
| Run # | 1 | 2 | 2 | 2 | 2 |
| Pressure (GPa) | 105.3 (9) | 125 (1) | 125 (1) | 125 (1) | 125 (1) |
| Synthesis Temperature (K) | 2400 (120) | 2260 (140) | 2260 (140) | 2260 (140) | 2260 (140) |
| Symmetry | Orthorhombic, <i>Pnma</i> , Z = 4 | | | Orthorhombic, <i>Imm2</i> , Z = 12 | |
| <i>a</i> (Å) | 5.08 (1) | 4.995 (4) | 5.006 (3) | 6.103 (4) | 6.08 (1) |
| <i>b</i> (Å) | 3.290 (2) | 3.277 (2) | 3.253 (2) | 9.098 (4) | 9.08 (1) |
| <i>c</i> (Å) | 6.146 (8) | 6.095 (2) | 6.100 (7) | 5.382 (1) | 5.380 (3) |
| <i>V</i> (Å ³) | 102.7 (3) | 99.8 (1) | 99.3 (1) | 298.8 (2) | 296.9 (7) |
| Reduction | | | | | |
| No. of measured, independent, and observed [<i>I</i> > 2σ(<i>I</i>)] reflections | 191, 110, 88 | 221, 123, 106 | 214, 110, 101 | 304, 259, 218 | 251, 217, 191 |
| <i>R</i> _{int} , <i>R</i> _{sigma} | 0.026, 0.033 | 0.019, 0.0213 | 0.0186, 0.0178 | 0.037, 0.039 | 0.024, 0.031 |
| Refinement | | | | | |
| <i>R</i> [<i>F</i> ² > 2σ(<i>F</i> ²)], <i>wR</i> (<i>F</i> ²), <i>S</i> | 0.062, 0.166, 1.05 | 0.048, 0.123, 1.04 | 0.038, 0.102, 1.175 | 0.077, 0.193, 1.131 | 0.057, 0.148, 1.066 |
| No. of reflections | 110 | 123 | 119 | 259 | 217 |
| No. of parameters | 10 | 10 | 19 | 26 | 26 |
| Δρ _{max} , Δρ _{min} (e Å ⁻³) | 2.83, -2.20 | 1.82, -2.03 | 1.37, -1.66 | 2.40, -2.88 | 2.18, -2.12 |
| Error on site occupancies | 5 % | 8 % | 3 % | 13 % | 18.0 % |



Supplementary Figures

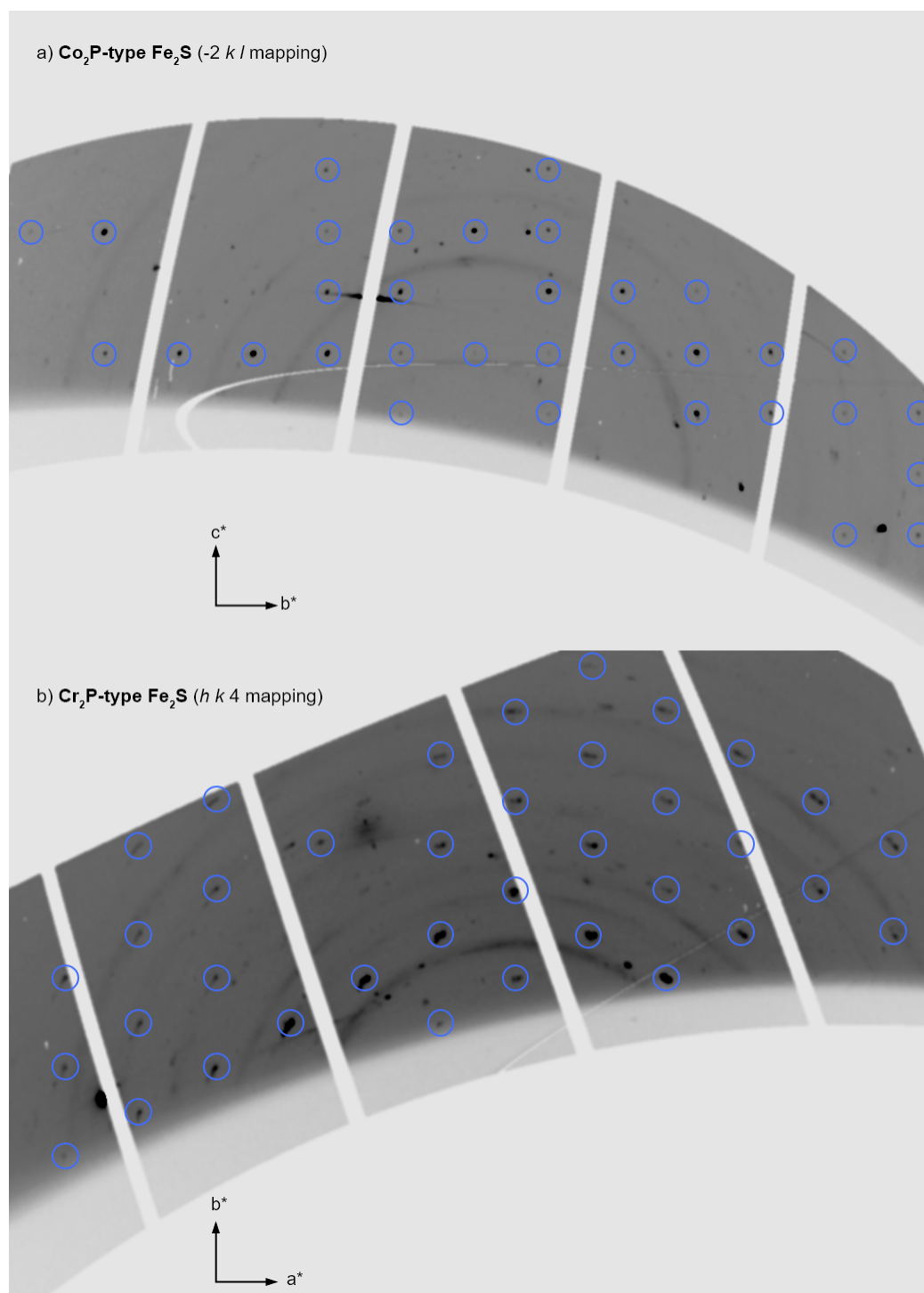


Figure S-1 Diffraction mappings of the lower-temperature (a) Co_2P -type and (b) Cr_2P -type Fe_2S polymorphs identified upon quenching from 125 GPa and 2300 K.

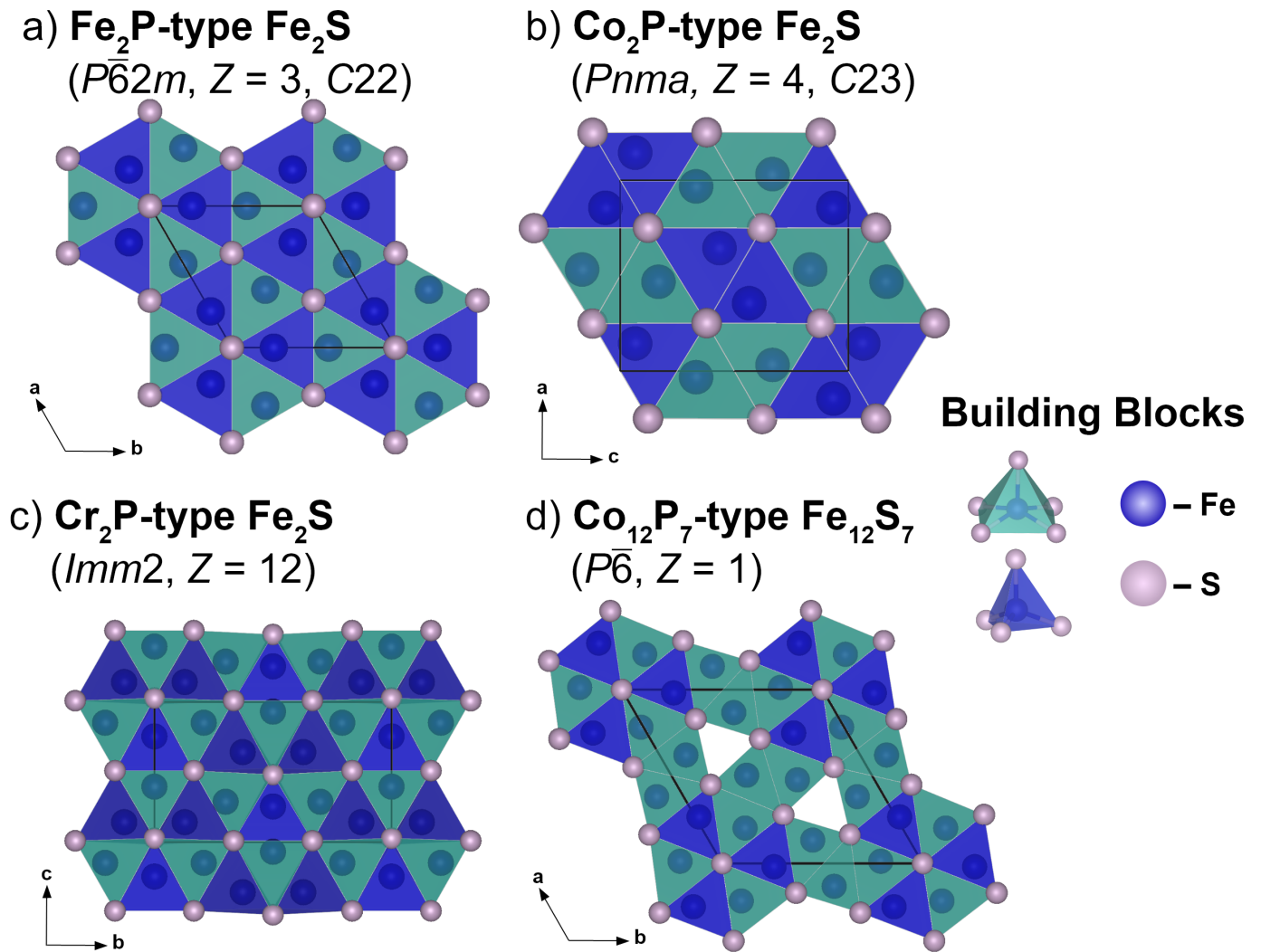


Figure S-2 Fe₂S and Fe₁₂S₇ crystal structures characterised in this study.

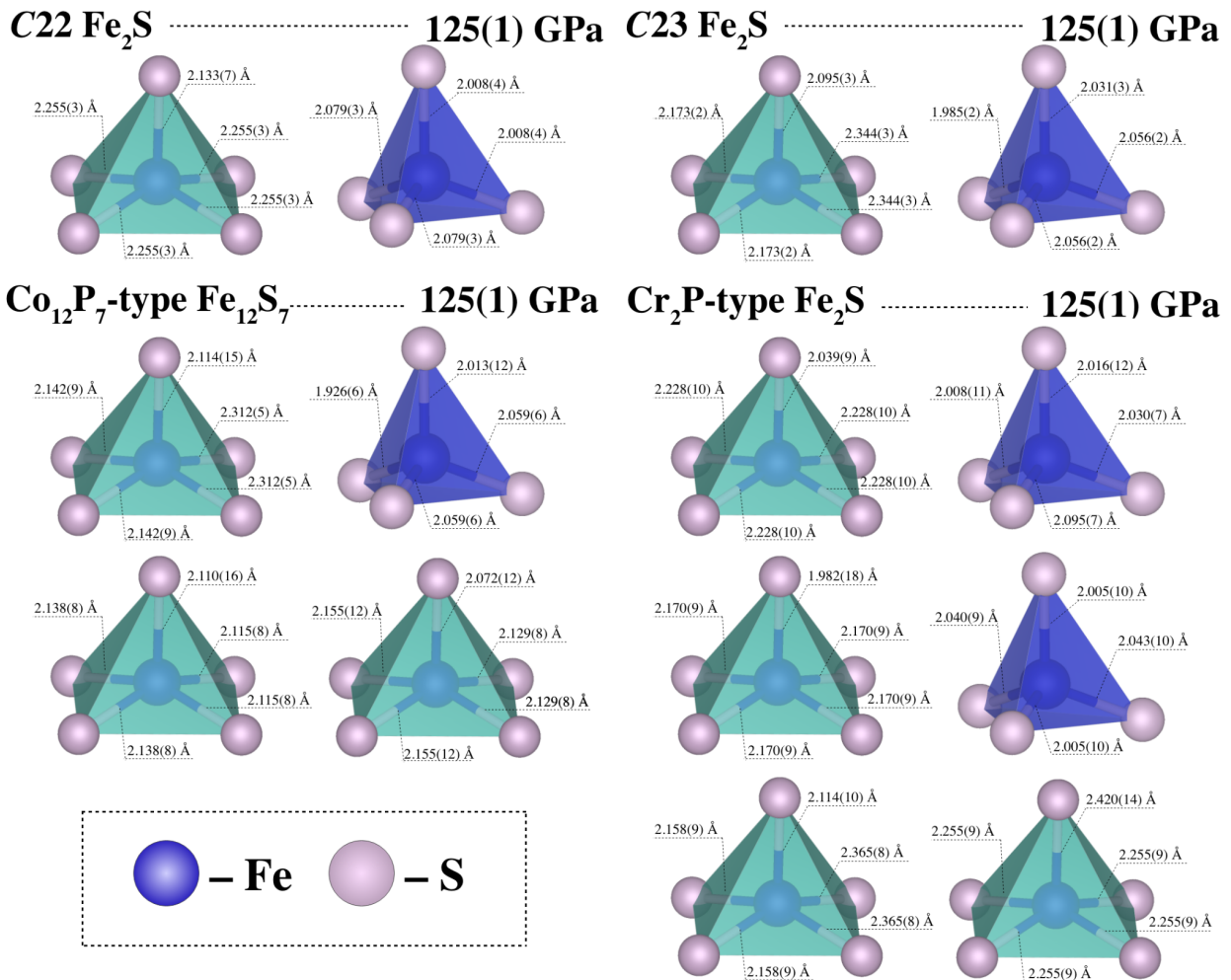


Figure S-3 Coordination polyhedra with labelled interatomic distances for C22 Fe₂S, C23 Fe₂S, Cr₂P-type Fe₂S, and Co₁₂P₇-type Fe₁₂S₇ measured at 125 GPa.

Appendices

Appendix A-1. Crystallographic information for C22 Fe₂S at 125(1) GPa.

Appendix A-2. Crystallographic information for C22 Fe₁₂S₇ at 105.3(9) GPa.

Appendix A-3. Crystallographic information for Cr₂P-type Fe₂S at 125(1) GPa.

Appendix A-4. Crystallographic information for C23 Fe₂S at 125(1) GPa.

Appendices A-1 to A-4 are Crystallographic Information Files (.cif) and can be downloaded at <https://doi.org/10.7185/geochemlet.2217>.



Supplementary Information References

- Artigas, M., Bacmann, M., Fruchart, D., Fruchart, R. (1996) La structure cristalline de Cr₂P: Distorsion orthorhombique de la structure hexagonale de type Fe₂P. *Journal of Solid State Chemistry* 123, 306–312. <https://doi.org/10.1006/jssc.1996.0184>
- Campbell, A.J., Seagle, C.T., Heinz, D.L., Shen, G., Prakapenka, V.B. (2007) Partial melting in the iron-sulfur system at high pressure: A synchrotron X-ray diffraction study. *Physics of the Earth and Planetary Interiors* 162, 119–128. <https://doi.org/10.1016/j.pepi.2007.04.001>
- Campbell, A.J., Danielson, L., Richter, K., Seagle, C.T., Wang, Y., Prakapenka, V.B. (2009) High pressure effects on the iron–iron oxide and nickel–nickel oxide oxygen fugacity buffers. *Earth and Planetary Science Letters* 286, 556–564. <https://doi.org/10.1016/j.epsl.2009.07.022>
- Chun, H.K., Carpenter, G.B. (1979) Redetermination of the Crystal Structure of Cr₁₂P₇. *Acta Crystallographica Section B: Structural Crystallography and Crystal Chemistry* 35, 30–33. <https://doi.org/10.1107/S0567740879002466>
- Dewaele, A., Belonoshko, A.B., Garbarino, G., Occelli, F., Bouvier, P., Hanfland, M., Mezouar, M. (2012) High-pressure–high-temperature equation of state of KCl and KBr. *Physical Review B* 85, 214105. <https://doi.org/10.1103/PhysRevB.85.214105>
- Dhahri, E. (1996) Etude des problèmes d'ordre et de stabilité dans les phases Ln₂M₁₂X₇ (terre rare - métal de transition - non métal). *Journal of Physics: Condensed Matter* 8, 4351. <https://doi.org/10.1088/0953-8984/8/24/004>
- Ellner, M., Mittemeijer, E.J. (2001) The Reconstructive Phase Transformation β-Co₂P → α-Co₂P and the Structure of the High-Temperature Phosphide β-Co₂P. *Zeitschrift für anorganische und allgemeine Chemie* 627, 2257–2260. [https://doi.org/10.1002/1521-3749\(200109\)627:9<2257::AID-ZAAC2257>3.0.CO;2-W](https://doi.org/10.1002/1521-3749(200109)627:9<2257::AID-ZAAC2257>3.0.CO;2-W)
- Heinz, D.L., Jeanloz, R. (1987) Measurement of the melting curve of Mg_{0.9}Fe_{0.1}SiO₃ at lower mantle conditions and its geophysical implications. *Journal of Geophysical Research: Solid Earth* 92, 11437–11444. <https://doi.org/10.1029/JB092iB11p11437>
- Lavina, B., Dera, P., Downs, R.T. (2014) Modern X-ray diffraction methods in mineralogy and geosciences. *Reviews in Mineralogy and Geochemistry* 78, 1–31. <https://doi.org/10.2138/rmg.2014.78.1>
- Prakapenka, V.B., Kubo, A., Kuznetsov, A., Laskin, A., Shkurikhin, O., Dera, P., Rivers, M.L., Sutton, S.R. (2008) Advanced flat top laser heating system for high pressure research at GSECARS: application to the melting behavior of germanium. *High Pressure Research* 28, 225–235. <https://doi.org/10.1080/08957950802050718>
- Prescher, C., Prakapenka, V.B. (2015) *DIOPTAS*: a program for reduction of two-dimensional X-ray diffraction and data exploration. *High Pressure Research* 35, 223–230. <https://doi.org/10.1080/08957959.2015.1059835>
- Rigaku Oxford Diffraction* (2018) CrysAlisPRO software system, v. 1.171.39.44a. Rigaku Corporation, Oxford, U.K.
- Sheldrick, G.M. (2014) *SHELXL-2014/7: Program for the Solution of Crystal Structures*. University of Göttingen, Göttingen, Germany.
- Sheldrick, G.M. (2015a) *SHELXT* - Integrated space-group and crystal-structure determination. *Acta Crystallographica Section A: Foundations and Advances* 71, 3–8. <https://doi.org/10.1107/S2053273314026370>
- Sheldrick, G.M. (2015b) Crystal structure refinement with *SHELXL*. *Acta Crystallographica Section C: Structural Chemistry* 71, 3–8. <https://doi.org/10.1107/S2053229614024218>
- Zurkowski C.C., Lavina B., Chariton S., Greenberg E., Prakapenka V.B., Campbell A.J. (2022) The crystal structure of Fe₂S at 90 GPa based on single-crystal X-ray diffraction techniques. *American Mineralogist* 107, 739–743. <https://doi.org/10.2138/am-2022-7973>

